ARTICLES
PUBLISHED ONLINE: 21 FEBRUARY 2010 | DOI: 10.1038/NNANO.2010.13
nature nanotechnology

An inorganic–organic proton exchange membrane for fuel cells with a controlled nanoscale pore structure

Saeed Moghaddam[1,2]*, Eakkachai Pengwang[2], Ying-Bing Jiang[3], Armando R. Garcia[4], Daniel J. Burnett[4], C. Jeffrey Brinker[3,5], Richard I. Masel[1] and Mark A. Shannon[1,2]*

Proton exchange membrane fuel cells have the potential for applications in energy conversion and energy storage, but their development has been impeded by problems with the membrane electrode assembly. Here, we demonstrate that a silicon-based inorganic–organic membrane offers a number of advantages over Nafion—the membrane widely used as a proton exchange membrane in hydrogen fuel cells—including higher proton conductivity, a lack of volumetric size change, and membrane electrode assembly construction capabilities. Key to achieving these advantages is fabricating a silicon membrane with pores with diameters of ~5–7 nm, adding a self-assembled molecular monolayer on the pore surface, and then capping the pores with a layer of porous silica. The silica layer reduces the diameter of the pores and ensures their hydration, resulting in a proton conductivity that is two to three orders of magnitude higher than that of Nafion at low humidity. A membrane electrode assembly constructed with this proton exchange membrane delivered an order of magnitude higher power density than that achieved previously with a dry hydrogen feed and an air-breathing cathode.

The ever-increasing demand for means of powering portable devices has generated a worldwide effort towards the development of high-energy-density power sources. Although advances in lithium-ion battery technology in recent years have provided higher power devices, this progress has not kept pace with the portable technologies, leaving a so-called power gap that is widely expected to grow in coming years. Micro fuel cell (MFC) technology, which has been under development for some time, has the potential to bridge this power gap. The energy density of the fuels used in MFCs exceeds that of batteries by an order of magnitude. However, efforts to harvest this high energy density have been hampered by issues concerning the fabrication, performance, reliability, size and cost of MFCs. At the heart of these issues are the polymer membranes, which show low conductivity at low humidity and a large volumetric size change with humidity that is a major source of failure and integration difficulties. The development of improved membrane materials and configurations has been the focus of research for decades, and success in this regard would represent a key step forward in low-temperature fuel cell technology. In addition, developing a membrane compatible with the manufacturing infrastructure within the semiconductor and micro-electro-mechanical systems (MEMS) silicon-processing industries would be a major technological breakthrough. To meet both of these objectives, we here introduce the concept of a surface nano-engineered, fixed-geometry, proton exchange membrane (PEM) that allows nearly constant proton conductivity over a wide range of humidity, with no changes in volume. In addition, our membrane is silicon-based, facilitating fabrication of membrane electrode assemblies (MEAs) and their further integration with microfabricated elements of MFCs.

The potential advantages of a silicon-based PEM over the widely used Nafion membrane have encouraged development efforts in recent years[1,2]. However, these have been largely unsuccessful due to difficulties in achieving two aims: robust processing of a nanoporous silicon membrane with uniform open pores, and self-assembly of molecules in torturous nanopores with extremely high aspect ratios. Perhaps more importantly, at low humidity the water meniscus becomes unstable within the pores in a homogeneous fixed-geometry membrane (Nafion pores shrink with decreasing humidity), leading to partial drying out. This drying out results in a significant increase in reactant crossover. To better understand the strategy behind our approach for overcoming the deficiencies of Nafion and significantly exceeding its proton exchange capacity, a brief overview of the existing hypothesis about the morphology of Nafion and its associated proton transport mechanisms is provided in the Supplementary Information.

Our strategy for the silicon-based membrane is to fabricate ~5–7-nm-diameter silicon pores and then assemble 3-mercaptopropyltrimethoxysilane (MPTMS; $SH–(CH_2)_3–Si–(OCH_3)_3$) molecules on the modified surface of the pores. The –SH end group of MPTMS is later oxidized to $–SO_3H$. The thickness of the MPTMS self-assembled monolayer (SAM) on silicon oxide is 0.8 ± 0.1 nm. An increase in the size of the head group after oxidation increases the thickness of the SAM to ~1 nm. The overall size of the pores after self-assembly therefore reduces to 3–5 nm. To enable high conductivity to be maintained at low humidities, an ultrathin conformal layer of silicon dioxide is deposited at the mouth of each of the larger silicon nanopores (Fig. 1), creating small apertures. Using the Kelvin equation, $\ln RH = -2\gamma V_m/rRT$, we calculated that a 1-nm-diameter water meniscus can be stable at 10% humidity, which is lower than the

[1]Department of Chemical and Biomolecular Engineering, University of Illinois at Urbana-Champaign, Urbana, Illinois 61801, USA, [2]Department of Mechanical Science and Engineering, University of Illinois at Urbana-Champaign, 1206 West Green Street, Urbana, Illinois 61801, USA, [3]Sandia National Laboratories, Albuquerque, New Mexico 87185, USA, [4]Surface Measurement Systems, Ltd, Allentown, Pennsylvania 18103, USA, [5]Department of Chemical and Nuclear Engineering, University of New Mexico, Albuquerque, New Mexico 87131, USA. *e-mail: saeedmog@illinois.edu; mshannon@illinois.edu

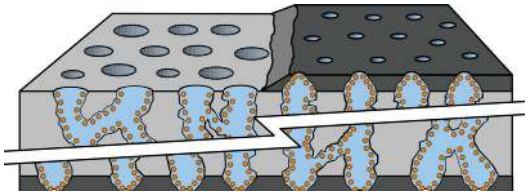

Figure 1 | Schematic of the membrane with functionalized pore wall and thin layers of porous silica on both sides of the membrane. The lateral scaling is stretched for clarity. Porous silicon membrane (light grey); silica layer (dark grey); self-assembled molecular monolayer (orange); water (cyan).

humidity level found in most practical applications of fuel cells. Although the specific conductivity of the silica layer can be relatively low, its overall contribution to total membrane resistance is negligible. In contrast to the uniform incorporation of nanoparticles (for example, SiO_2) into Nafion to enhance its hydration properties (see a recent review by Devanathan[3]), or homogeneous inorganic–organic membranes such as the one recently developed by Athens and colleagues[4], this asymmetric membrane construction maintains hydration without a detrimental effect on proton conductivity.

Porous silicon membrane

The porous silicon membrane is fabricated in two main steps. First, a silicon membrane is made using the process described in the Methods. Anodization is then used to create the pores within the silicon membrane. A typical two-cell[5] anodization process, in which the wafer is installed between two electrolyte baths, leaves a layer of non-porous silicon on the back side of the membrane. (A review of the challenges involved in the fabrication of open through-holes can be found in the work of Föll and colleagues[6].) To open up the pores, the remaining silicon layer should be etched using Freon plasma. As a result of variations in the thickness of the remaining silicon layer on a single membrane and over different membranes on a wafer, as well as the pore penetration depth (Fig. 2b), the silicon layer is etched in some areas, thus exposing the porous silicon. The exposed porous silicon is then etched at a much faster rate (3–5 times) than the silicon, resulting in localized thinning of the membrane. This issue makes the fabrication of thin membranes impractical. In addition to the thickness issue, our analysis of the composition of the membrane using time-of-flight secondary ion mass spectroscopy (ToF–SIMS) showed a significant rise in the presence of fluorine, particularly towards the back side of the membrane.

To overcome these issues, we developed a self-terminating method that leads to the production of membranes with uniform, open-ended pores, in a single step. The process involves the deposition of a layer of chromium and gold on the back side of the membrane using a magnetron sputtering system (pressure, 5×10^{-2} torr; power, 300 W d.c.) in argon gas. The back-side chromium/gold layer is wired directly to the anode electrode to provide an electrical path by which the electrons can exit the silicon membrane once the pores penetrate to the back side of the membrane. When the pores open up, at any location, the chromium layer is etched and the gold layer delaminates, resulting in local electrical discontinuity and therefore termination of anodization. Because the gold layer is not etched, it maintains the electrical connectivity of the rest of the membrane to the circuit. The gold delamination process occurs gradually over the entire wafer until the pores on all membranes are opened. This event appears as a sudden rise in process voltage, as shown in Fig. 2c. The finite increase in voltage arises from the continuation of the anodization process beyond the edges of the membrane into the bulk silicon. Interestingly, the gold layer left outside the membrane can be used as the anode electrode. The cathode electrode is also a chromium/gold layer deposited on the front side of the wafer before etching the nitride layer (both chromium/gold and nitride layers are etched in one patterning step).

Hydroxylation of the pore surface

Following the anodization process, the membrane is left in deionized (DI) water for a few hours to clean the anodization electrolyte from the pores. As the Fourier transfer infrared (FTIR) spectra

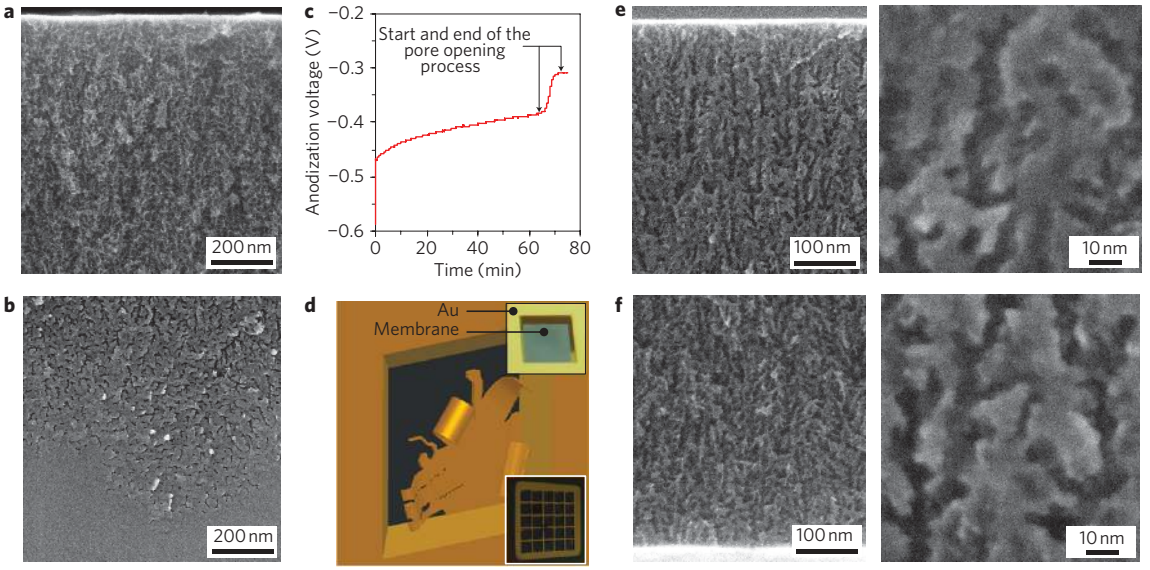

Figure 2 | Fabrication process for the porous silicon membrane. a,**b**, Cross-section of the membrane fabricated in a two-cell anodization bath: front side (**a**) and 1–2 μm from the back side of the membrane (**b**). **c**, Variation of the anodization voltage at constant current showing a sudden rise in voltage when the electrolyte reaches the chromium layer. **d**, Schematic of the gold layer peel-off process when the chromium layer is etched. Insets: actual images of two silicon dies, one with a single membrane and another with a 5 × 5 matrix of ~2 × 2 mm^2 membranes after completion of the process. The remaining gold layer outside the membrane area is later used as a current collector in a complete MEA. **e**,**f**, Cross-sections of the membrane fabricated using the self-terminating process developed in this study: front (**e**) and back (**f**) sides of the membrane.

of the membrane of Fig. 3a suggests, the pore wall is covered with SiH_x ($x = 1$–3) hydrophobic surface species (the absorption bands were assigned by Glass and colleagues[7]). To successfully conduct silane-based self-assembly within the membrane, the surface of the pores needs to be converted to hydrated silica[8–12]. This was achieved in two steps. First, the membrane was partially oxidized at a low temperature (300 °C) in an O_2 furnace. Although temperatures close to 600 °C are required to desorb surface hydride species[13,14], processing at such a temperature level is not practical due to the resultant significant changes in membrane morphology and membrane fracturing. The morphology of porous silicon is known to change at temperatures above 350–450 °C (refs 14,15) due to changes in the crystalline dimensions (that is, coarsening of the porous silicon texture[16,17]). These changes result in a significant decrease in the specific surface area[14]. However, no distinct texture coarsening has been observed at 300 °C (refs 16,17). The oxidized membrane spectrum (Fig. 3b) shows that all $Si–H_x$ vibrational stretch modes have shifted to 2,260 cm^{-1}, with a low-intensity tail extending towards lower frequencies, suggesting that the backbone of the silicon atoms is targeted by oxygen, and that the maximum degree of oxidation to $–O_3SiH$ (corresponding to absorption at 2,260 cm^{-1} frequency[18–20]) has occurred. The lower-frequency tail also indicates the presence of a relatively small population of $–O_ySiH_x$ surface species. Leaving the membrane in DI water after the oxidation step results in the insertion of oxygen into the Si–H bonds and the creation of SiOH surface species. As a result, the absorption bands at 2,260 and 876 cm^{-1} associated with $–O_3SiH$ stretching and bending modes, respectively, disappear, and absorption at 3,743 cm^{-1}, assigned to isolated SiOH species[21], intensifies together with the Si–O asymmetric stretching vibrations at 1,200 to 1,000 cm^{-1} assigned to the siloxane network (Fig. 3c). The broad absorption band centred at ~3,500 cm^{-1} corresponds to the overlapping of the O–H stretching bands of hydrogen-bonded water (H–O–H···H) and SiO–H stretching of surface silanols hydrogen-bonded to molecular water (SiO–H···H_2O; ref. 22). These results suggest the creation of the well-hydrated silica pore surface needed for the subsequent self-assembly step.

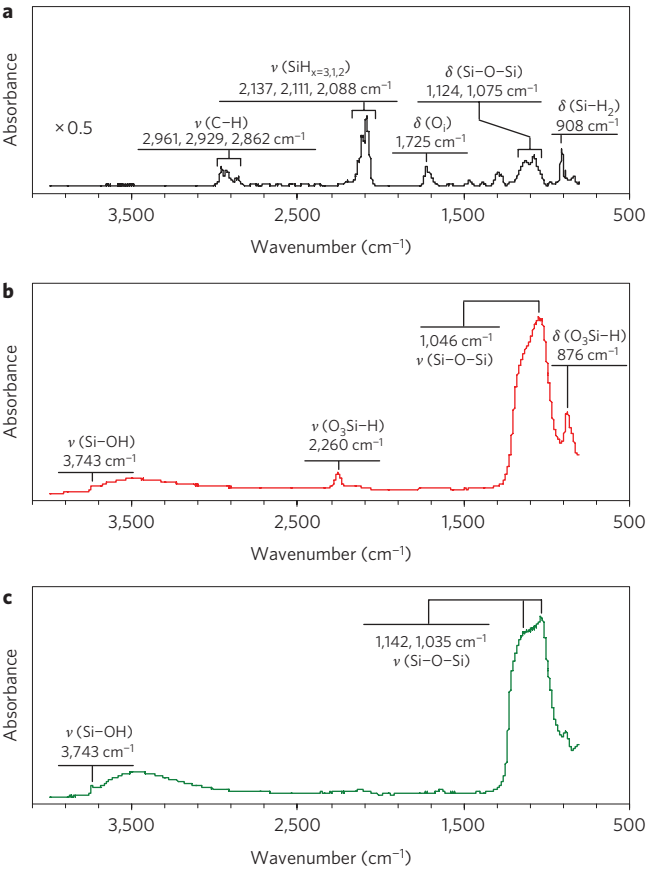

Figure 3 | FTIR spectra of the membrane at different stages of pore surface modification. a, Anodized membrane left in DI water for a few hours. **b**, Oxidized membrane at 300 °C in atmospheric O_2. **c**, Oxidized membrane after room-temperature DI water soak for 2 days (no further changes were observed in the spectra after 4 days). Based on the drop in intensity of the 876 cm^{-1} absorption peak during the DI soak process, we assign this unsettled peak[18,27,28] to the bending mode of $–O_3SiH$, because the decrease in intensity of this mode is accompanied by that of the known peak 2,260 cm^{-1} and increase in 3,743 cm^{-1} intensity. Assignment of this peak to other modes such as Si–O stretching and the OH bending of the SiOH group[28] coupling of Si–H and Si–O–Si motions[18] does not seem accurate, because the intensities of the Si–O, Si–O–Si and SiOH bonds do not decline during the two-day DI soak process. We have determined that the 1,142 cm^{-1} peak developed during the two-day DI soak process is due to surface oxide.

Sulphonation of the pore surface

Owing to the large surface area and high aspect ratio of the pores, a reactor was constructed (Fig. 4a) to continuously supply an ~1 mM solution of MPTMS to one end of the pores and extract the solvent from their opposite end. Details of the functionalization process are provided in the Methods. This procedure enabled uniform functionalization of the hydroxyl groups within the membrane (estimated to be ~5 sites nm^{-2}) as confirmed by ToF–SIMS with depth profiling (shown in Fig. 4b). The –SH end group of the MPTMS molecule was then oxidized to $–SO_3H$ in dilute nitric acid and, finally, the membrane was maintained in a large volume of DI water for 24 h to diffuse out the nitric acid and hydrate the pores.

Reduction of the pore mouth diameter

To create a thin hydrophilic silica aperture at the mouth of the pores, we used plasma-directed atomic layer deposition (PD–ALD)[23]. Unlike conventional ALD, in PA–ALD, a remote plasma (instead of water vapour exposure) is used to activate the surface. Because both the plasma Debye length and the radical mean free path greatly exceed the pore diameter, surface activation and silica deposition are confined to the immediate external surface of the membrane pores, with no deposition on the internal pores. Successive oxygen plasma and tetramethyl orthosilicate (TMOS) exposure steps using an argon carrier gas resulted in an ~2-nm-thick silica layer. The interior of the pores within the silica layer were then functionalized with MPTMS. The maximum diameter of the pores at the two surfaces of the membrane is ~2 nm, as estimated from scanning electron microscopy (SEM) and analysis of water desorption isotherms (Fig. 5).

Fabrication of the membrane electrode assembly

The last fabrication stage of the MEA is spray painting of the anode and cathode catalysts on the membrane (Fig. 5d). A catalyst ink with an 18 wt% ratio of Nafion ionomer 1100 EW (from Solution Technology) to platinum black (from Alfa Aesar) was prepared in DI water and isopropyl alcohol (IPA). Direct spray painting of the catalyst ink onto the membrane is straightforward, because the membrane does not swell and wrinkle as the catalyst solution comes into contact with the membrane surface. The membrane was set on a hot plate at 85 °C during spraying. As mentioned previously, and shown in Fig. 2d, chromium/gold layers already deposited on both sides of the die are used as current collectors. The catalyst layer overlaps with the chromium/gold electrode around the edges of the membrane and

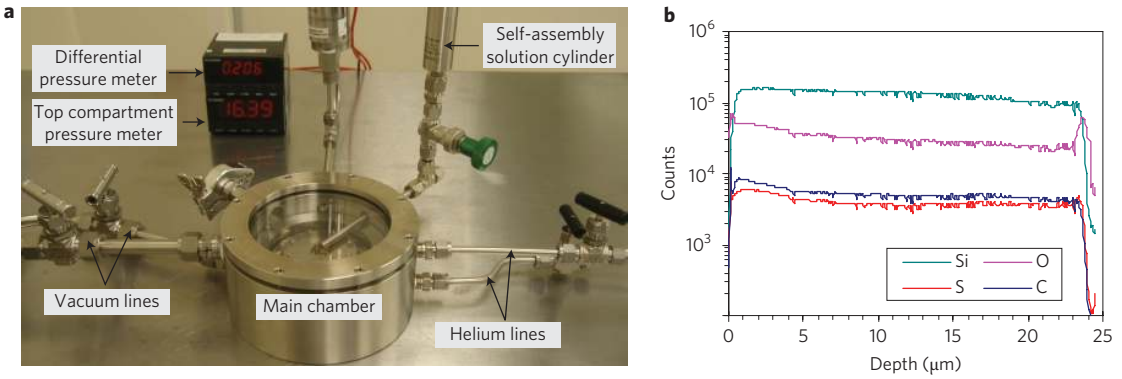

Figure 4 | Self-assembly of functional groups on the membrane wall of the pores. **a**, Membrane functionalization reactor with a main chamber consisting of top and bottom compartments between which the membranes wafer is installed. **b**, ToF-SIMS results (phase depth profile using a 22 kV Au^+ analysis beam and a 2 kV Cs^+ sputtering beam), showing the composition of a functionalized 24-μm-thick membrane.

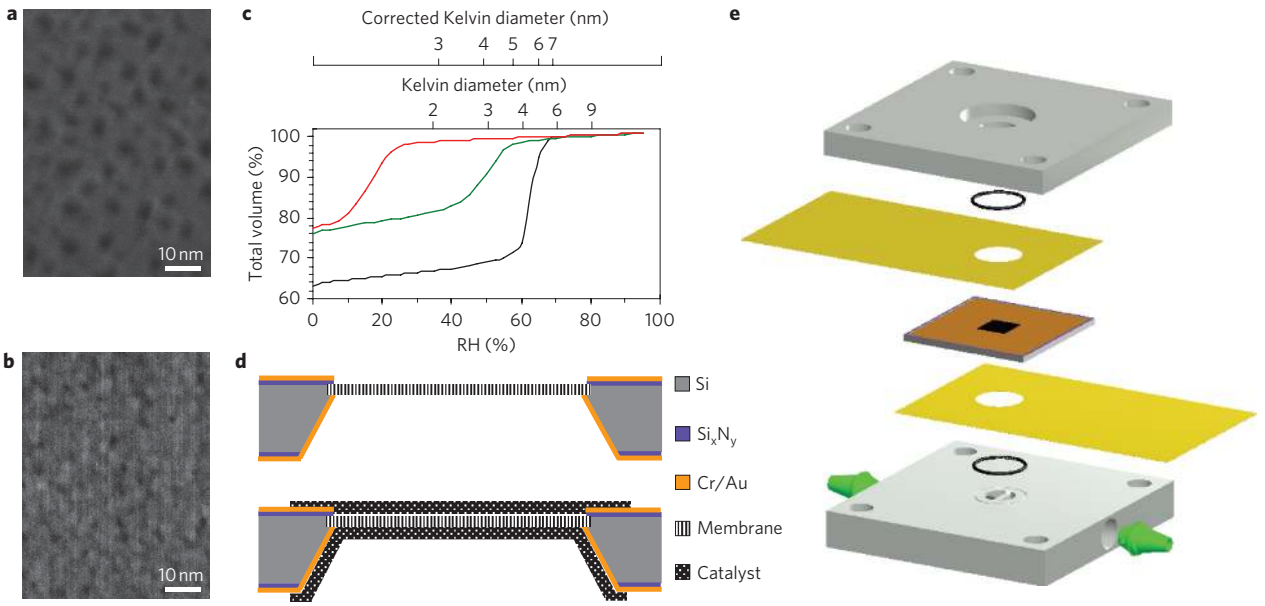

Figure 5 | Membrane pore size characterization and details of the MEA and its test package. **a**,**b**,Top view of two membranes without (**a**) and with (**b**) the PA-ALD silica layer. **c**, Water desorption isotherms of the membrane (determined using DVS-Advantage 1 machine (Surface Measurement Systems) on samples with 25 membranes, shown in Fig. 2d, at 25 °C) before functionalization (black), after functionalization (green) and after application of the PD-ALD silica layer and subsequent functionalization (red). The graph also shows the corresponding Kelvin diameter as well as the corrected Kelvin diameter based on the t-curve for a silica surface of Hagymassy and colleagues[29]. Note that using silica t-curve results in a small error in the case of the functionalized pores. **d**, Cross-sectional schematic of a single membrane within its silicon die before and after application of the catalyst layers. **e**, Three-dimensional schematic of the MEA test package showing two Teflon blocks sandwiching the MEA, with two 50-μm-thick gold foils positioned in between, coming into contact with the anode and cathode electrodes to provide an electrical connection to the outside of the package. Hydrogen is supplied to the anode through a hole within the bottom Teflon block, and an opening in the top Teflon block exposes the cathode to air. The internal electrical resistance of the package was measured to be 7 mΩ. This was measured by replacing the device die with a gold foil and using the four-probe measurement technique.

provides electrical connectivity. The platinum loading in the catalyst layers was 7 mg cm^{-2}.

Characterization

All tests were conducted on the MEA in a configuration most relevant to MFCs, in which no auxiliary equipment for conditioning the membrane as well as the supply gases is desired; that is, dry hydrogen is supplied to the anode and the cathode is air-breathing at room temperature (~25 °C). The test package (Fig. 5e) was left in an environmental chamber to simulate different ambient humidity levels (the uncertainty in the humidity measurement was ±2%). The membrane proton conductivity was measured using the four-probe technique (using a Solartron 1287). The results (MEA-1) are compared (Fig. 6) with another silicon-based MEA but without the PD–ALD-deposited silica layers (MEA-2), as well as with another MEA based on DuPont Nafion PFSA NRE-211 membrane (MEA-3) with a nominal thickness of 25 μm. This MEA was fabricated by sandwiching Nafion between two stainless steel foils with 2×2 mm^2 square openings aligned during adhesive bonding of the layers. The exposed 2×2 mm^2 Nafion membrane was subsequently brush-painted with catalyst. Before discussing the various differences between the developed membrane and Nafion, we should mention that adding the silica layer resulted in ~25% decline in the maximum conductivity of the PS–PEM, from ~0.11 to 0.08 S cm^{-1}. This significant decline is most likely due to the closure of some of the smaller membrane pores after the

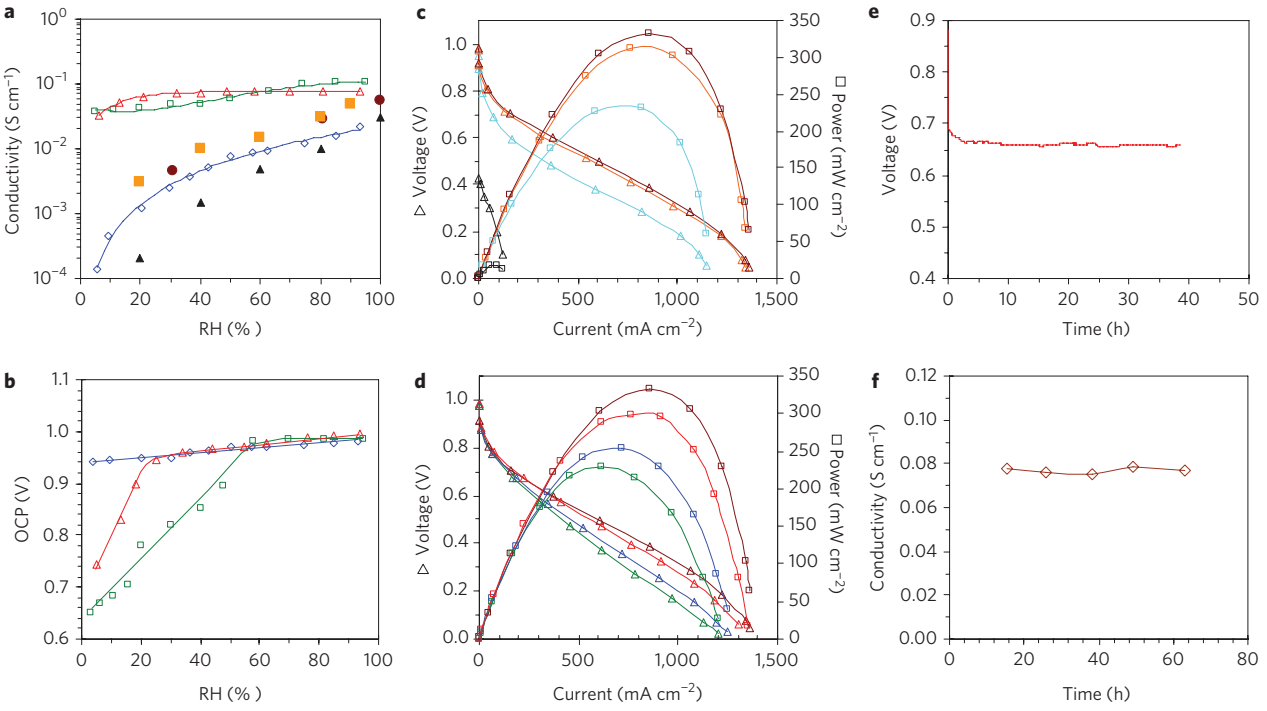

Figure 6 | Performance of the PS-PEM membrane and MEA using a dry hydrogen feed and an air-breathing cathode. The tests were conducted at room temperature (~25 °C) with a hydrogen supply of 1.2 to 1.5 times the stoichiometric ratio and less than 1 kPa pressure. A single cell membrane was used in all tests (additional information on characterization of micro fuel cells can be found in the work of Moghaddam and colleagues[30]). **a**, Proton conductivity as a function of humidity: PS-PEM with the PD-ALD silica layers, MEA-1 (red); PS-PEM without the silica layers, MEA-2 (green); Nafion NRE-211 hot-pressed at 100 °C, MEA-3 (blue); N-117 heat-treated at 105 °C (black triangles) and 30 °C testing temperature[24]; N-117 at 30 °C (ref. 25; orange squares); N-117 at 30 °C (ref. 26; brown circles). **b**, OCP as a function of humidity: MEA-1 (red); MEA-2 (green); MEA-3 (blue). **c**, Voltage–current and power characteristics of MEA-1 at moderate and low humidity ambient: 70% (brown); 55% (orange); 25% (cyan); comparison with Pichonat and Gauthier-Manuel's[2] PS-PEM (black). **d**, Effect of high humidity on MEA-1 performance: 95% (green); 92% (blue); 85% (red); 70% (brown). **e**, Life test results at an operating current of 150 mA cm^{-2} and 75% humidity. **f**, Membrane proton conductivity measured at different time periods after starting the test at 150 mA cm^{-2} operating current and 75% humidity.

PD–ALD and subsequent self-assembly processes, rather than impeded proton mobility at the smaller entrance and exit of the pores, considering the small thickness of the silica layers.

Other than this observation, the results show that the conductivity of the MEA-1 membrane is almost constant down to ~20% humidity, at which point it starts to decline significantly. A similar trend is seen for the MEA-2 membrane, but with the decline beginning at a higher humidity level (50–60%). This difference is expected, because a smaller pore diameter allows the water meniscus to remain stable at a lower humidity ambient. The decline in humidity levels beyond this thermodynamic equilibrium condition leads to partial drying out of the pores and an increase in crossover, as is made evident by the drop in open circuit potential (OCP) (Fig. 6b). Overall, the data suggest a nearly humidity-independent conductivity, as long as the vapour pressure at the membrane/ambient interface remains below the ambient saturated vapour pressure, so that the ambient vapour condenses within the pores, keeping them filled with water. This fundamentally different property of the silicon-based membrane compared to that of Nafion, in which the pores shrink at low ambient humidity, is a major contributing factor to the difference in conductivity between these two membranes. When the Nafion pores shrink, the amount of bulk-like water at the centre of the pores sharply declines. Shrinkage, along with a reduction in the interconnectivity of the water clusters, is responsible for the exponential decay in Nafion conductivity.

The conductivities of the MEA-1 and MEA-2 membranes are factors of 3.5 and 4.8, respectively, greater than that of the MEA-3 membrane at 95% humidity. However, we should mention that the MEA-3 membrane has passed through a hot-pressing step at 100 °C (as part of its fabrication process), which is widely known to adversely affect Nafion conductivity. Our data on the MEA-3 membrane at high humidity closely matches data on a N-117 membrane heat-treated at 105 °C in a study by Sone and colleagues[24]. At low humidity, however, the conductivity of the MEA-3 membrane is an order of magnitude higher than that of the heat-treated N-117. Data on non-heat-treated N-117 membranes from Zawodzinski and colleagues[25] and Sumner and colleagues[26] are provided in Fig. 6a for further comparison. The data suggest a conductivity of ~0.06 S cm^{-1} at 95% humidity for non-heat-treated Nafion, which is moderately less than the 0.08 and 0.11 S cm^{-1} conductivities associated with MEA-1 and MEA-2 membranes, respectively. Understanding the reasons behind the higher conductivity of the PS–PEM compared to Nafion requires detailed characterization of the PS–PEM, as well as a more concrete understanding of the Nafion structure and mechanisms of proton conductivity within its pores. Other than the morphological differences between the two membranes, as well as the pore wall properties, the difference in number density of the sulphonate groups on the pore wall and the length and chemistry of their pendant groups are among the parameters that can affect proton mobility.

The current–voltage (I–V) performance of MEA-1 at different humidity levels is provided in Fig. 6c,d. The MEA delivered a maximum power density of 332 mW cm^{-2} at 70% humidity. However, operation at lower humidities led to a decline in performance, primarily due to an increase in activation overpotential losses

resulting from an increase in charge transfer resistance within the catalyst layer due to Nafion dryout. Although the greater loss and its effect on the maximum power density was minimal at 55% humidity, further reducing the humidity to 25% resulted in a significant activation loss that led to ~30% decline in maximum output power. Operation at high humidity levels also led to performance degradation (Fig. 6d) as a result of partial water flooding of the cathode catalyst due to a low water evaporation rate. In addition to the *I*–*V* performance tests, an MEA was subjected to continuous operation at 150 mA cm^{-2} for 40 h. Other than a drop of 0.018 V during the first 5 h of operation (Fig. 6e), believed to be mainly due to the system reaching a steady state, the device showed an additional drop of 0.007 V over the remainder of the test period (0.18 mV h^{-1}). To determine if changes in the membrane proton conductivity were responsible for the observed drop in potential, a second test was carried out in which the membrane conductivity was measured frequently after periods of operation (Fig. 6f). The results did not show any statistically significant change in membrane conductivity. The membrane conductivity does not therefore seem to be responsible for the decline observed in MEA performance.

Conclusions

We have reported the development of a next-generation PEM/MEA. The fixed geometry of the pores and asymmetric construction of the membrane allow high proton conductivity at low humidity levels. Owing to the many advantages of this PEM/MEA, we envision that this technology can simplify the fabrication and operation of small fuel cells. The fabrication processes developed to create the PS–PEM provide a versatile route to nanostructuring membranes with tailored properties for optimum performance. The ability to modify the surface of this dimensionally stable membrane opens up vast opportunities to fine-tune the characteristics of the membranes (for example, water and fuel transport through the membrane), enabling the development of better fuel cells. The technologies presented in this work can potentially be used for low-crossover membranes for liquid fuels, membranes for use in above ambient operating temperatures (120–140 °C), anion exchange membranes, and so on. In addition, the known geometry of the pores and the ability to systematically control the pore surface chemistry with SAMs provide a unique opportunity to enhance our understanding of the physics of proton transport and its relation to pore size and surface properties.

Methods

Silicon membrane. Fabrication of the silicon membranes begins with KOH etching of a p-doped <100> silicon wafer. A 0.8-μm-thick low-pressure chemical vapour deposition (LPCVD) nitride layer was used as a protection mask in KOH solution. The nitride layer on the back side of the membrane was patterned and etched using a Freon plasma. The exposed silicon areas were then etched in KOH until a membrane thickness of 24±2 μm was reached. The nitride layer on the front side of the membrane was subsequently patterned and etched to expose the silicon. In membranes with an additional metal layer on the front side, the patterning step was followed by wet etching of the metal layer and then Freon plasma etching of the nitride layer.

Functionalization. The membrane die was installed within a fixture between the top and bottom compartments of the functionalization set-up. This arrangement allowed continuous extraction of the depleted solvent from the bottom of the membrane pores while the solute-rich solvent was supplied over the membrane. A typical process run involved evacuating the chamber and purging with helium multiple times to remove condensed water from the pores. Excess water results in self-polymerization of the MPTMS molecules and clogging of the pores (note that surface adsorbed water remains on the surface). MPTMS in benzene solution was then supplied to the solution reservoir on top of the membrane. Although the top chamber was charged with helium and the vacuum and helium lines connected to it were closed, the lines connected to the bottom compartment were opened slightly to maintain a slow flow of dry helium. The process was continued until the top reservoir was emptied of solution.

Received 26 October 2009; accepted 18 January 2010; published online 21 February 2010

References

1. Gold, S., Chu, K.-L., Lu, C., Shannon, M. A. & Masel, R. I. Acid loaded porous silicon as a proton exchange membrane for micro-fuel cells. *J. Power Sources* **135,** 198–203 (2004).
2. Pichonat, T. & Gauthier-Manuel, B. Realization of porous silicon based miniature fuel cells. *J. Power Sources* **154,** 198–201 (2006).
3. Devanathan, R. Recent developments in proton exchange membranes for fuel cells. *Energy Environ. Sci.* **1,** 101–119 (2008).
4. Athens, G. L., Ein-Eli, Y. & Chmelka, B. F. Acid-functionalized mesostructured aluminosilica for hydrophilic proton conduction membranes. *Adv. Mater.* **19,** 2580–2587 (2007).
5. Lehmann, V. *Electrochemistry of Silicon: Instrumentation, Science, Materials and Applications* (Wiley-VCH, 2002).
6. Föll, H., Carstensen, J. & Frey, S. Porous and nanoporous semiconductors and emerging applications. *J. Nanomater.* **2006,** 1–10 (2006).
7. Glass, J. A., Wovchko, E. A. & Yates, J. T. Reaction of atomic hydrogen with hydrogenated porous silicon-detection of precursor to silane formation. *Surf. Sci.* **348,** 325–334 (1996).
8. Silberzan, P., Leger, L., Ausserre, D. & Benattar, J. J. Silanation of silica surfaces. A new method of constructing pure or mixed monolayers. *Langmuir* **7,** 1647–1651 (1991).
9. Tripp, C. P. & Hair, M. L. An infrared study of the reaction of octadecyltrichlorosilane with silica. *Langmuir* **8,** 1120–1126 (1992).
10. Le Grange, J. D., Markham, J. L. & Kurkjian, C. R. Effects of surface hydration on the deposition of silane monolayers on silica. *Langmuir* **9,** 1749–1753 (1993).
11. Tripp, C. P. & Hair, M. L. Direct observation of the surface bonds between self-assembled monolayers of octadecyltrichlorosilane and silica surfaces: a low-frequency IR study at the solid/liquid interface. *Langmuir* **11,** 1215–1219 (1995).
12. Onclin, S., Ravoo, B. J. & Reinhoudt, D. N. Engineering silicon oxide surfaces using self-assembled monolayers. *Angew. Chem. Int. Ed.* **44,** 6282–6304 (2005).
13. Gupta, P., Colvin, V. L. & George, S. M. Hydrogen desorption kinetics from monohydride and dihydride species on silicon surfaces. *Phys. Rev. B* **37,** 8234–8243 (1988).
14. Halimaoui, A., Campidelli, Y., Larre, A. & Bensahel, D. Thermally induced modifications in the porous silicon properties. *Phys. Status Solidi* **190,** 35–40 (1995).
15. Sugiyama, H. & Nittono, O. Microstructure and lattice distortion of anodized porous silicon layers. *J. Crystal Growth* **103,** 156–163 (1990).
16. Herino, R., Perio, A., Barla, K. & Bomchil, G. Microstructure of porous silicon and its evolution with temperature. *Mater. Lett.* **2,** 519–523 (1984).
17. Labunova, V., Bondarenkoa, V., Glinenkoa, I., Dorofeeva, A. & Tabulinaa, L. Heat treatment effect on porous silicon. *Thin Solid Films* **137,** 123–134 (1986).
18. Gupta, P., Dillon, A. C., Bracker, A. S. & George, S. M. FTIR studies of H_2O and D_2O decomposition on porous silicon surfaces. *Surf. Sci.* **245,** 360–372 (1991).
19. Ogata, Y., Niki, H., Sakka, T. & Iwasaki, M. Oxidation of porous silicon under water vapor environment. *J. Electrochem. Soc.* **142,** 1595–1601 (1995).
20. Gorbanyuk, T. I., Evtukh, A. A., Litovchenko, V. G., Solnsev, V. S. & Pakhlov, E. M. Porous silicon microstructure and composition characterization depending on the formation conditions. *Thin Solid Films* **495,** 134–138 (2006).
21. Iler, R. K. *The Chemistry of Silica* (Wiley, 1976).
22. Brinker, C. J. & Scherer, G. W. *Sol–Gel Science: The Physics and Chemistry of Sol–Gel Processing* (Academic Press, 1990).
23. Jiang, Y.-B. *et al.* Sub-10-nm-thick microporous membranes made by plasma-defined atomic layer deposition of a bridged silsesquioxane precursor. *J. Am. Chem. Soc.* **129,** 15446–15447 (2007).
24. Sone, Y., Ekdunge, P. & Simonsson, D. Proton conductivity of Nafion 117 as measured by a four-electrode AC impedance method. *J. Electrochem. Soc.* **143,** 1254–1259 (1996).
25. Zawodzinski, T. A. *et al.* A comparative study of water uptake by and transport through ionomeric fuel cell membranes. *J. Electrochem. Soc.* **140,** 1981–1985 (1993).
26. Sumner, J. J., Creager, S. E., Ma, J. J. & DesMarteau, D. D. Proton conductivity in Nafion 117 and in a novel *bis*[(perfluoroalkyl)sulfonyl]imide ionomer membrane. *J. Electrochem. Soc.* **145,** 107–110 (1998).
27. Lucovsky, G., Yang, J., Chao, S. S., Tyler, J. E. & Czubatyj, W. Oxygen-bonding environments in glow-discharge-deposited amorphous silicon–hydrogen alloy films. *Phys. Rev. B* **28,** 3225–3233 (1983).
28. Uchino, T., Sakka, T. & Iwasaki, M. Interpretation of hydrated states of sodium silicate glasses by infrared and Raman analysis. *J. Am. Ceram. Soc.* **74,** 306–313 (1991).

29. Hagymassy, J., Brunauer, S. & Mikhail, R. S. Pore structure analysis by water vapor adsorption. I. t-curves for water vapor. *J. Colloid Interface Sci.* **29,** 485–491 (1969).
30. Moghaddam, S., Pengwang, E., Lin, K. Y., Masel, R. I. & Shannon, M. A. Millimeter-scale fuel cell with onboard fuel and passive control system. *J. MEMS* **17,** 1388–1395 (2008).

Acknowledgements

Financial support for the UIUC team was provided by the Defense Advanced Research Projects Agency (DARPA). C.J.B. was supported through the US Department of Energy, Office of Basic Energy Sciences (grant DE-FG02-02-ER15368) and, Division of Catalysis and Division of Materials Sciences and Engineering. Y.B.J. was supported through the Sandia National Laboratories LDRD program. This work was carried out in part in the Frederick Seitz Materials Research Laboratory Central Facilities, University of Illinois, which are partially supported by the US Department of Energy under grant nos DE-FG02-07ER46453 and DE-FG02-07ER46471. The authors would like to thank T. Spila, R. Haasch and V.V. Mainz for their assistance with the ToF–SIMS, XPS and NMR analysis, and G. Mensing for reviewing the paper. The help of R. Morgan and J. Jihyung in preparing catalysts is also appreciated.

Author contributions

S.M. conceived the asymmetric PEM and MEA designs and conceived and performed the self-terminating pore fabrication process as well as modification of the pore surface properties. S.M. performed characterization tests and data analysis. S.M. and M.A.S. discussed the results. E.P. KOH-etched the silicon membranes and deposited the chromium/gold layers. Y.B.J. and C.J.B. performed the PD–ALD work and wrote the corresponding section in the paper. A.R.G. and D.J.B. conducted water desorption tests on some of the membranes. S.M. wrote the paper. M.A.S., C.J.B. and R.I.M commented on the paper.

Additional information

The authors declare no competing financial interests. Supplementary information accompanies this paper at www.nature.com/naturenanotechnology. Reprints and permission information is available online at http://npg.nature.com/reprintsandpermissions/. Correspondence and requests for materials should be addressed to S.M. and M.A.S.